Electronic Supplementary Material (ESI) for Journal of Materials Chemistry A.

Supporting Information

Electrocatalytic hydrogenation coupling oxidation using water in a highly efficient paired cell enabled by oxygen defect-rich layered double hydroxide

*Jing Ren[a], Jikang Wang[a], Zixian Li[a], Chenjun Ning[a], Wenjing Cao[a], Shaoquan Li[a], Geoffrey I. N. Waterhouse[d], Lirong Zheng[e], Dermot O'Hare[f], Yufei Zhao[abc]**

((Optional Dedication))

[a]State Key Laboratory of Chemical Resource Engineering, Beijing University of Chemical Technology, 100029 Beijing, P. R. China.

E-mail: zhaoyufei@mail.buct.edu.cn

[b]Qingyuan Innovation Laboratory, Quanzhou, Fujian, China

[c]Quzhou Institute for Innovation in Resource Chemical Engineering, Quzhou, Zhejiang, P. R.

[d]School of Chemical Sciences, The University of Auckland, Auckland 1142, New Zealand

[e]Beijing Synchrotron Radiation Facility Institute of High Energy Physics, Chinese Academy of Sciences, 100049 Beijing, P. R. China

[f]Chemistry Research Laboratory, Department of Chemistry, University of Oxford, Mansfield Road, Oxford OX1 3TA, United Kingdom

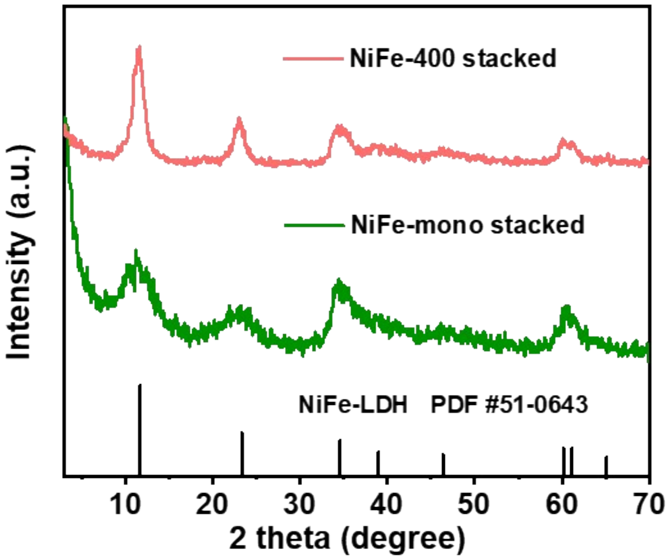

Figure S1. XRD patterns for NiFe-mono and NiFe-400 after redispersion in an aqueous Na_2CO_3 solution.

After re-dispersion in a Na_2CO_3 aqueous solution, both NiFe-mono and NiFe-400 existed in the form of stacks, evidenced by the characteristic (00*l*) diffraction peaks of multilayer NiFe-LDH. Results confirmed that both NiFe-mono and NiFe-400 were LDH materials.

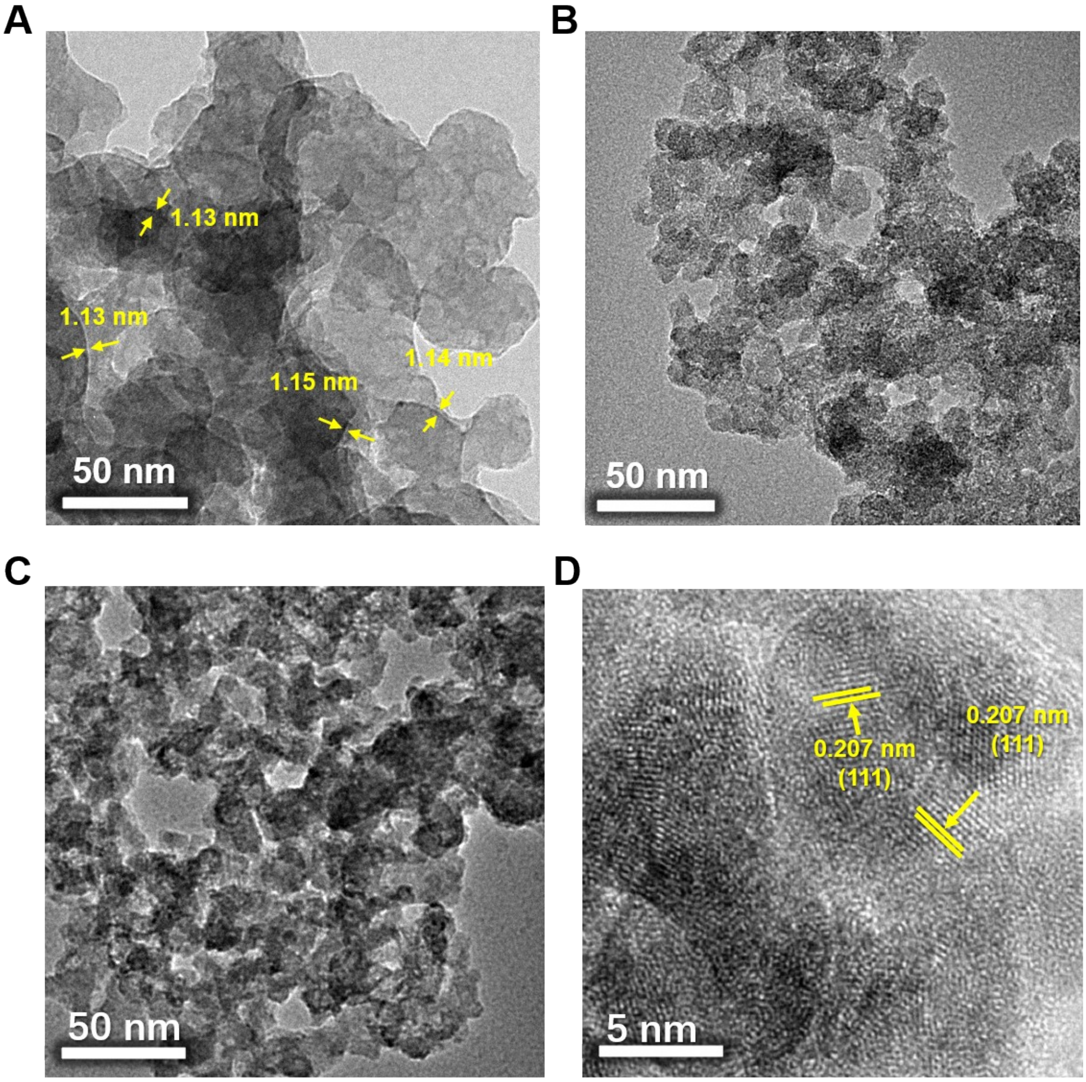

Figure S2. HRTEM images of (A) NiFe-mono; (B) NiFe-300; (C) and (D) NiFe-500.

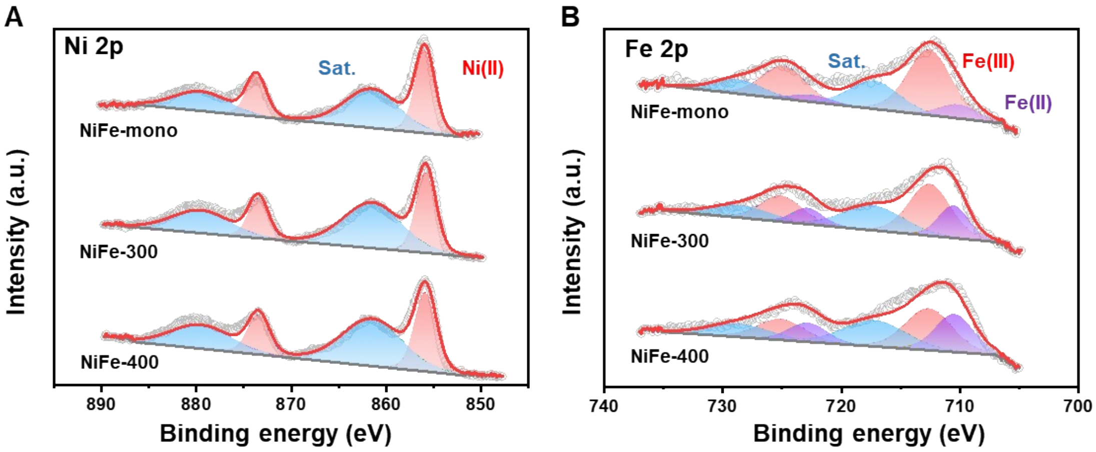

Figure S3. (A) Ni 2p and (B) Fe 2p XPS spectra of NiFe-mono, NiFe-300, and NiFe-400, respectively.

The Ni 2p spectra only showed two peaks with binding energies at 855.8 and 873.4 eV correspond to the Ni^{2+} $2p_{3/2}$ and Ni^{2+} $2p_{1/2}$, respectively[1, 2]. For Fe 2p spectra, the simultaneous existence of Fe^{2+} (710.4 and 722.8eV) and Fe^{3+} (712.5 and 725.0 eV) can be detected[3, 4], and the concentration ratio of the two metal ions gradually increases (NiFe-LDH, $Fe^{2+}/Fe^{3+} = 0.19$; NiFe-300, $Fe^{2+}/Fe^{3+} = 0.46$; NiFe-400, $Fe^{2+}/Fe^{3+} = 0.74$), indicating that Fe is gradually reduced with the increase of reduction temperature.

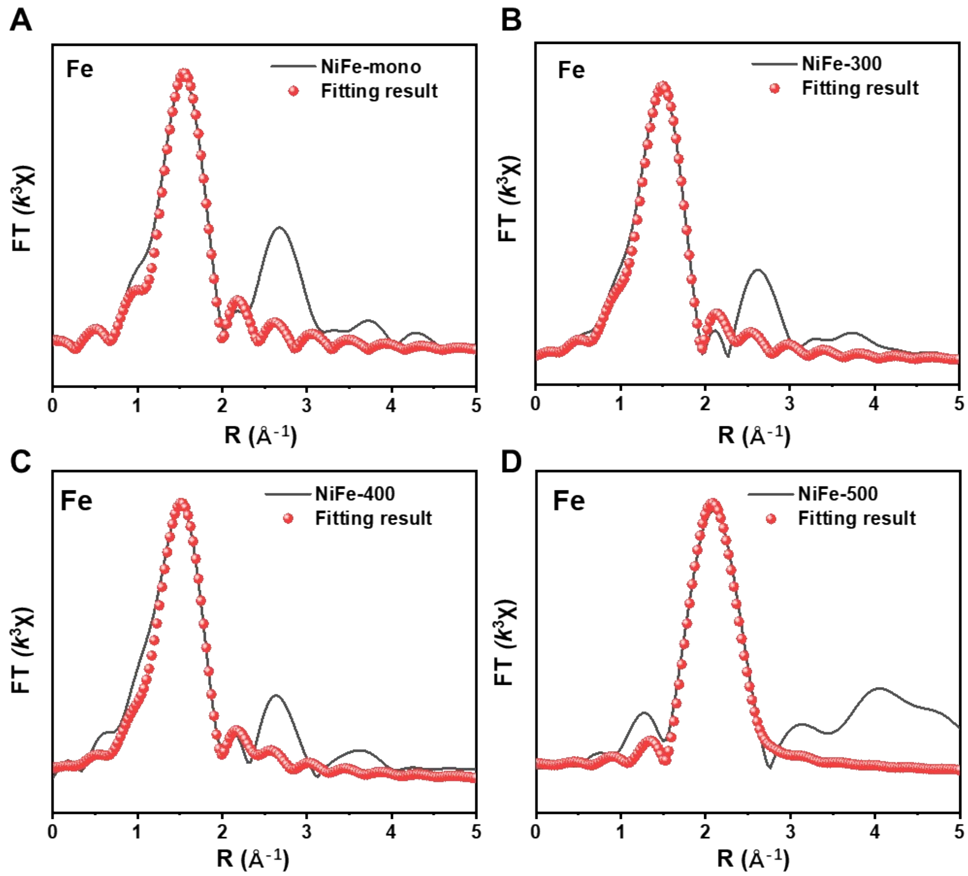

Figure S4. Fe K-edge *R*-space plots with corresponding fitting results for (A) NiFe-mono; (B) NiFe-300; (C) NiFe-400 and (D) NiFe-500.

Table S1. Local structure parameters around Fe for NiFe-mono and NiFe-*x* estimated by EXAFS analysis.

sample	**shell**	***N***	***R*(Å)**	**σ^2(10^{-3} Å^2)**	***R*-factor(10^{-3})**
NiFe-mono	Fe-O	5.43	2.00	4.42	4.39
NiFe-300	Fe-O	4.95	1.96	7.50	5.04
NiFe-400	Fe-O	3.96	1.97	9.00	12.3
NiFe-500	Fe-M	7.94	2.49	7.75	12.4

N = coordination number; *R* = average distance between absorber and backscatter atoms; σ^2 = Debye-Waller factor.

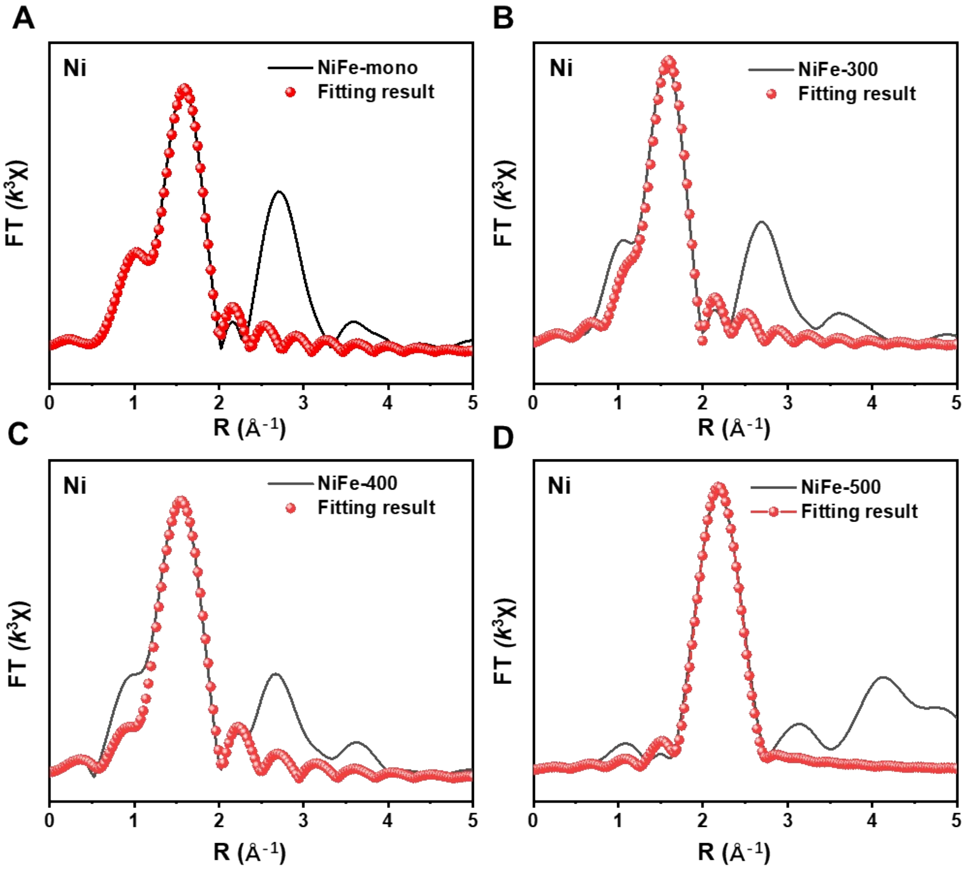

Figure S5. Ni K-edge *R*-space plots with corresponding fitting results for (A) NiFe-mono; (B) NiFe-300; (C) NiFe-400 and (D) NiFe-500.

Table S2. Local structure parameters around Ni for NiFe-mono and NiFe-*x* estimated by EXAFS analysis.

Sample	**Shell**	***N***	***R*(Å)**	**σ^2(10^{-3} Å^2)**	***R*-factor(10^{-3})**
NiFe-mono	Ni-O	5.42	2.05	4.65	4.02
NiFe-300	Ni-O	5.21	2.03	5.50	17.0
NiFe-400	Ni-O	4.64	2.02	5.00	10.0
NiFe-500	Ni-M	8.24	2.50	7.55	8.52

N = coordination number; *R* = average distance between absorber and backscatter atoms; σ^2 = Debye-Waller factor.

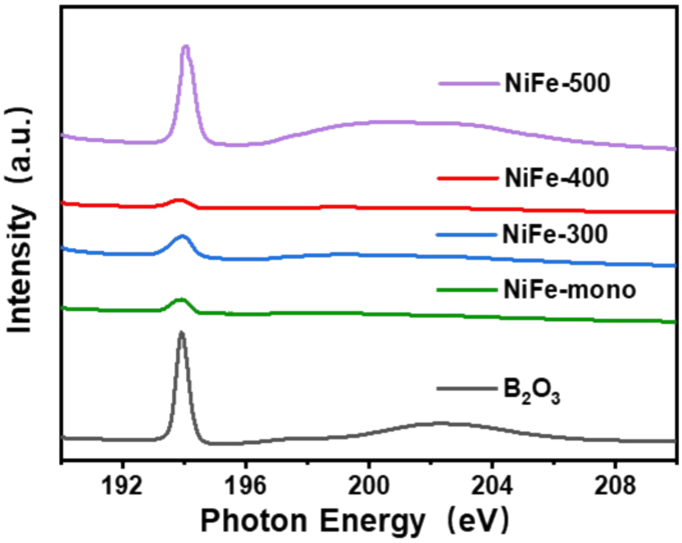

Figure S6. B K-edge XANES spectra for NiFe-mono, NiFe-300, NiFe-400 and NiFe-500. Data for the B_2O_3 is also provided as a reference.

B K-edge X-ray absorption near edge spectroscopy (XANES) was used to explore the chemical environment of B during the thermal reduction of NiFe-mono. As shown in Figure S5, the speciation of B in NiFe-mono, NiFe-300, NiFe-400 and NiFe-500 were very similar showing the presence of B^{3+} in B-O bonding environment. No evidence for B-Ni or B-Fe bonds were seen in the spectra, demonstrating that B-O bonds were very stable in the LDH-derived samples.

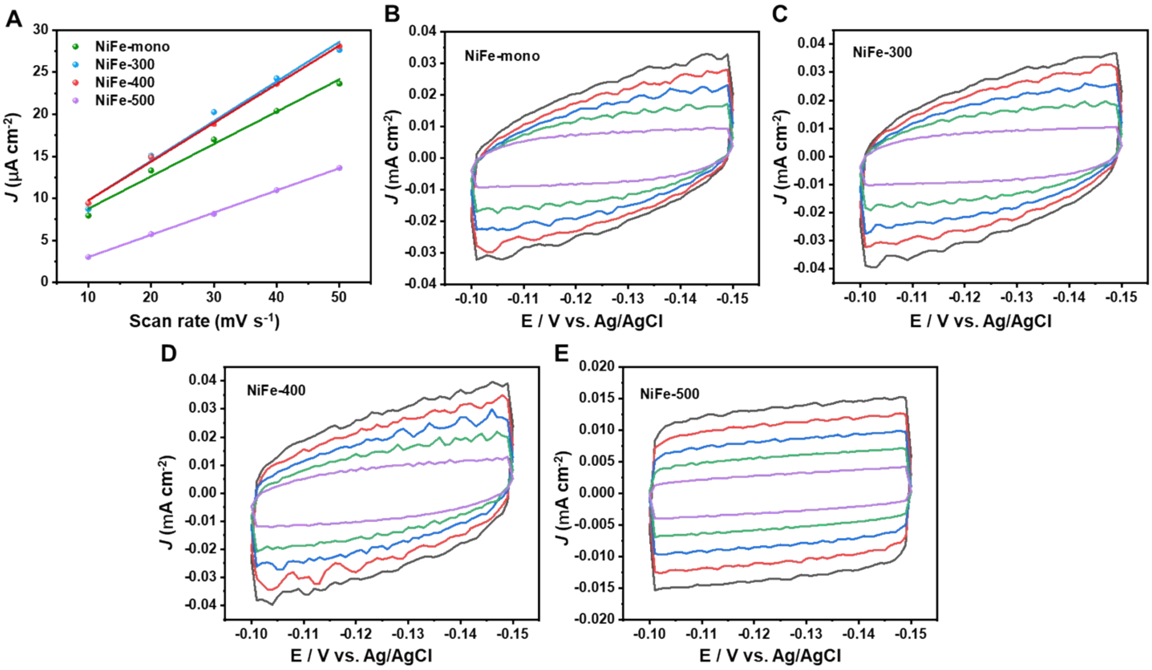

Figure S7. (A) Plots of current density versus scan rate for NiFe-mono, NiFe-300, NiFe-400 and NiFe-500 respecting ECSA, corresponding CV curves for (B) NiFe-mono, (C) NiFe-300, (D) NiFe-400 and (E) NiFe-500 in 1.0 M KOH electrolyte with 10 mM *p*-NP.

Electrochemically active surface area (ECSA) measurements were used to estimate the intrinsic activities of NiFe-mono, NiFe-300, NiFe-400 and NiFe-500 for *p*-NP reduction. Cyclic voltammetry (CV) measurements at different scan rates (10, 20, 30, 40, 50 mV s^{-1}) in a non-Faradaic region were used to calculate the electric double-layer capacitance value (C_{dl}) of the catalysts, with the C_{dl} values then used to obtain the ECSA values. The ECSA of the four catalysts followed the order NiFe-300 (47.04 mF cm^{-2}) > NiFe-400 (46.02 mF cm^{-2}) > NiFe-mono (38.43 mF cm^{-2}) > NiFe-500 (26.40 mF cm^{-2}).

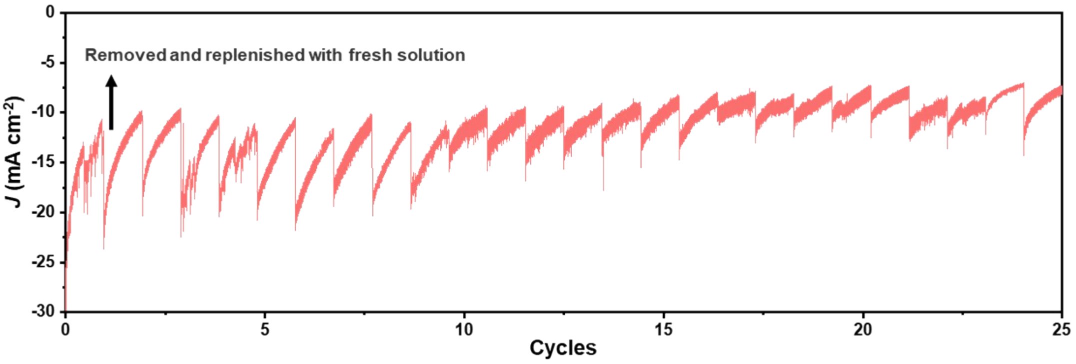

Figure S8. Current density for *p*-NP electrocatalytic reduction by NiFe-400 at -1.0 V *vs.* Ag/AgCl. The *p*-NP solution was replenished periodically.

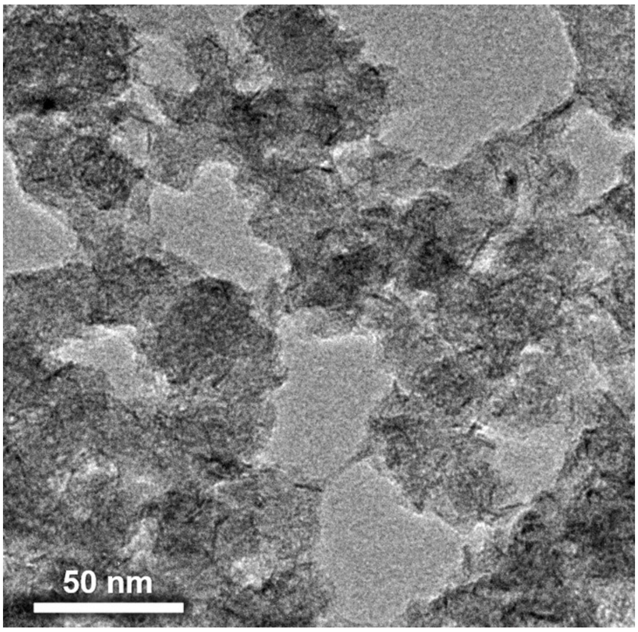

Figure S9. HRTEM image of NiFe-400 after the electrocatalytic reduction of *p*-NP.

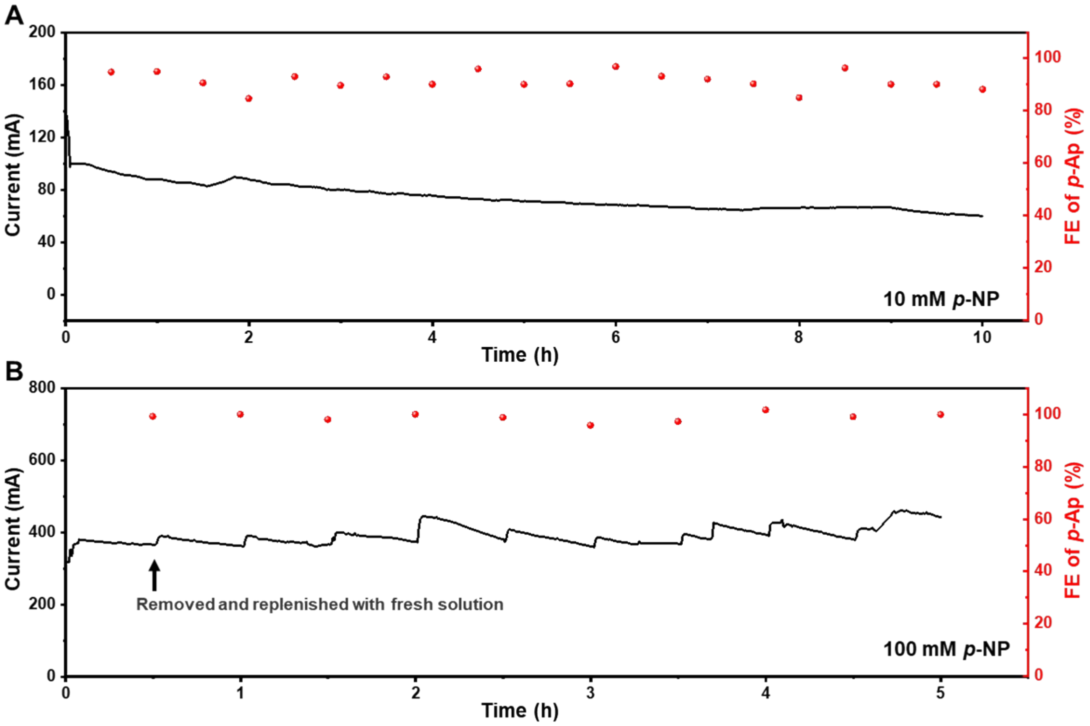

Figure S10. I-t curves for the continuous operation of the flow cell at (A) 10 mM *p*-NP for 10 h and (B) 100 mM *p*-NP for 5 h at 2.0 V of full voltage using NiFe-400. FEs toward *p*-AP are also shown.

Table S3. Comparison of electrocatalytic reduction reactivity of organic substrates with different catalyst.

Catalyst	Type of electrocatalytic hydrogenation	Reduction Agent	FE for product (%)	Reactant concentration (mM)	Reference
Co-F NW	Quinolines to 1,2,3,4-tetrahydroquinolines	H_2O	-	10	*Nat Commun 13, 5297 (2022)*[5]
$MoNi_4$	Quinolines to 1,2,3,4-tetrahydroquinolines	H_2O	80	10	*Chin J Catal 42, 1983-1991 (2021)*[6]
1T-rich MoS_2	furfural to furfuryl alcohol	H_2O	-	20	*Green Chem 24, 7974-7987 (2022)*[7]
Ag/C	5-hydroxymethylfurfural to 2,5-bis(hydroxymethyl)furan	H_2O	96.2	20	*Green Chem 21, 6210-6219 (2019)*[8]
Ru_1Cu (SAA)	5-hydroxymethylfurfural to 2,5-dihydroxymethylfuran	H_2O	87.5	100	*Angew Chem Int Ed 61, e202209849 (2022)*[9]
PtRhAu	Lignin monomer guaiacol to 2-methoxycyclohexanol	H_2O	58	120	*J Am Chem Soc 143, 17226-17235 (2021)*[10]
RhPtRu	Guaiacol to methoxy-cyclohexanes	H_2O	62.8	100	*Green Chem 24, 142-146 (2022)*[11]
Pd@CF	Benzaldehyde to benzyl alcohol	H_2O	≥ 90.2	20	*Adv Funct Mater, 2214588 (2023)*[12]
Pd–Mo	4-nitrostyrene to 4-vinylaniline	H_2O	78.3	10	*J Mater Chem A 11, 7505-7512 (2023)*[13]
CoP	Nitroarene to azoxy-, azo- and amino-aromatics	H_2O	99	20	*Natl Sci Rev 7, 285-295 (2019)*[14]
Co_3S_{4-x} NS	Nitroarenes to Aminoarenes	H_2O	-	20	*CCS Chem 3, 507-515 (2021)*[15]
Ru-PA/NF	*p*-nitrophenol to *p*-aminophenol	H_2O	73	5	*Int J Hydrogen Energy 47, 2187-2199 (2022)*[16]
NiB_x	*p*-nitrophenol to *p*-aminophenol	H_2O	≥ 99	10	*Angew Chem Int Ed 58, 9155-9159 (2019)*[17]
$Cu(OH)_2$	*p*-nitrophenol to *p*-aminophenol	$NaBH_4$	96.8	10	*ACS Catal 12, 1545-1557 (2022)*[18]
$CuCo_2O_4$/NF	*p*-nitrophenol to *p*-aminophenol	H_2O	89	20	*ACS Catal 12, 58-65 (2021)*[19]
NiFe-400	***p*-nitrophenol to *p*-aminophenol**	**H_2O**	**≥ 97**	**100**	**This work**

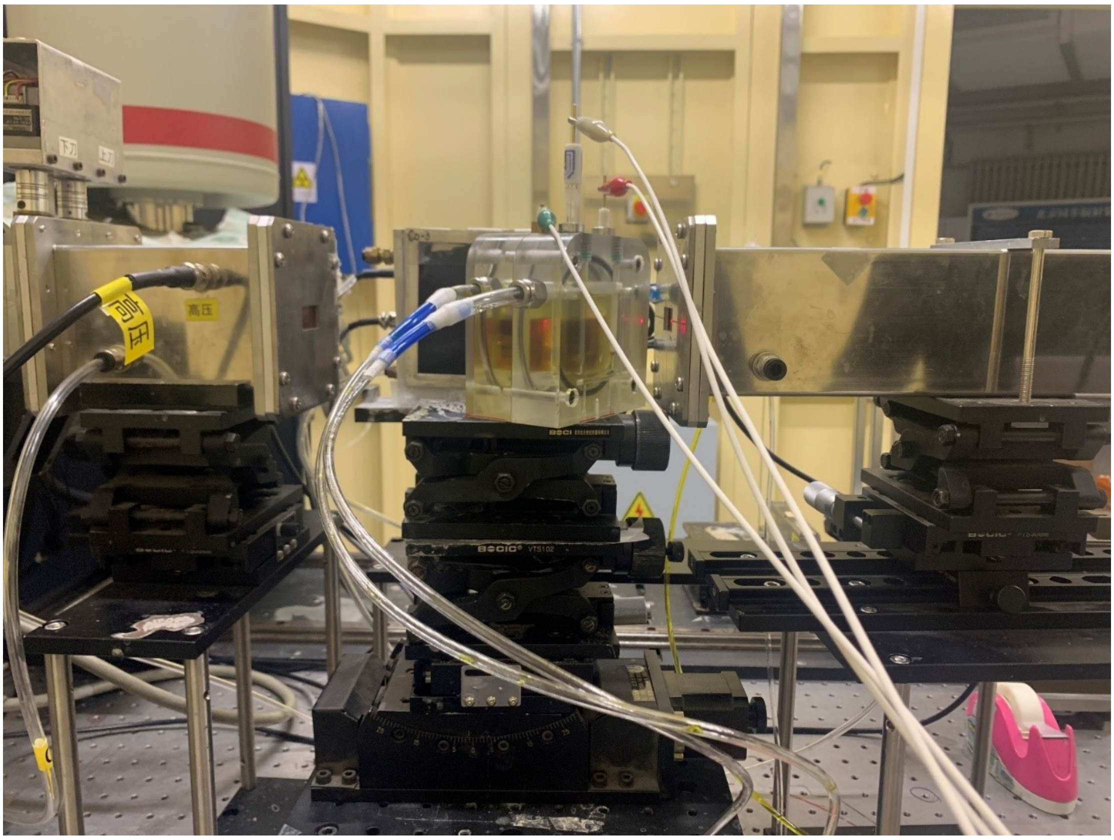

Figure S11. Photograph of the device used for *in-situ* XAFS measurements during electrocatalytic *p*-NP reduction.

In the context of *in-situ* XAFS testing, the first step involves collecting spectra of the electrode material in 1M KOH solution with and without 10 mM *p*-NP, respectively, while no applied voltage is present. Next, the suitable voltage is chosen for performing I-T testing, during which the spectra of the electrode material involved in the real-time *p*-NP reduction reaction are able to be gathered.

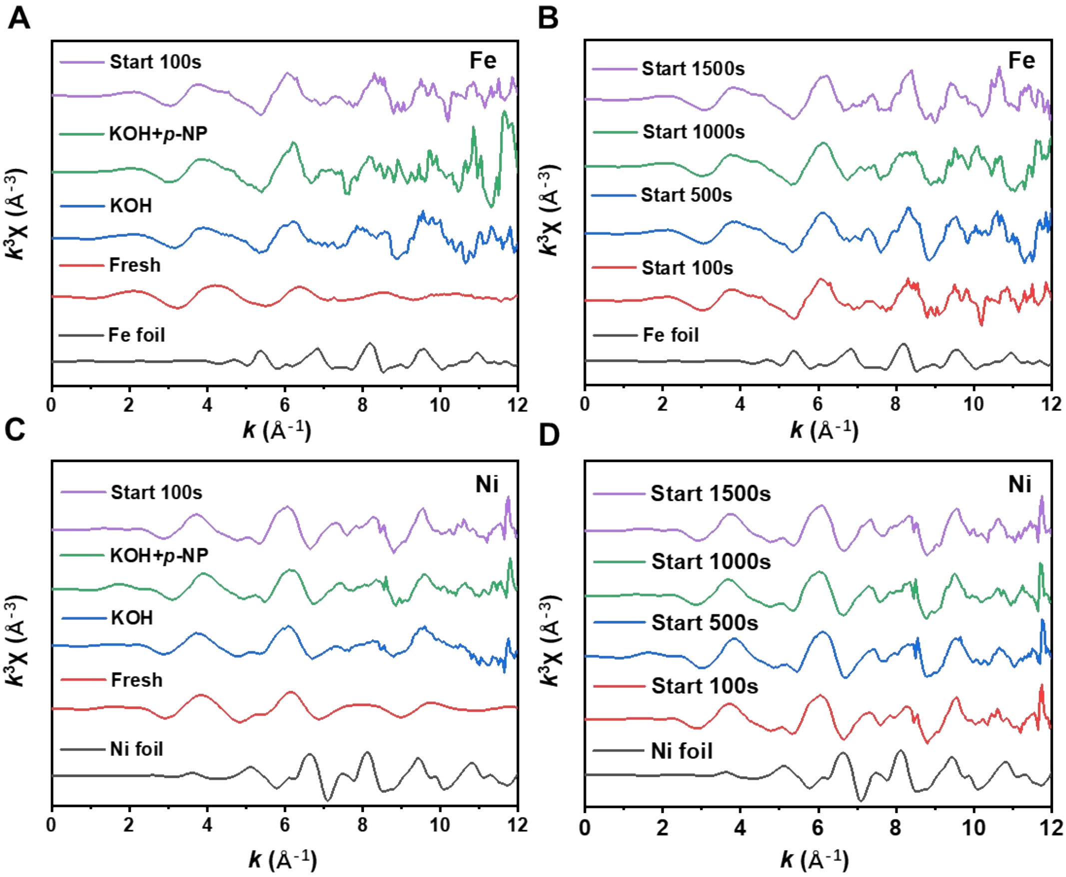

Figure S12. *In-situ* Fe K-edge EXAFS oscillation functions $k^3\chi(k)$ for (A) NiFe-400 before and (B) during *p*-NP reduction. *In-situ* Ni K-edge EXAFS oscillation functions $k^3\chi(k)$ for (C) NiFe-400 before and (D) during *p*-NP reduction.

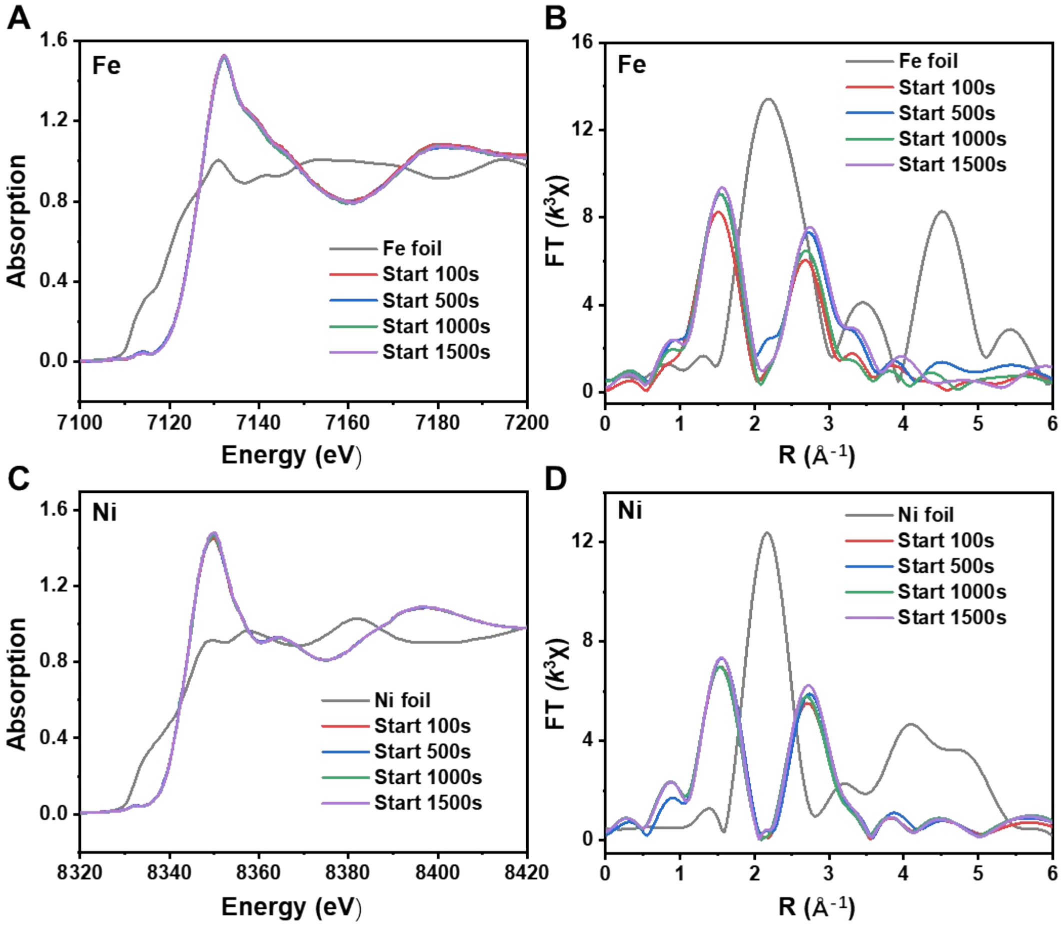

Figure S13. *In-situ* XAFS for the electrocatalytic reduction of *p*-NP by NiFe-400. (A) Fe K-edge XANES and (B) corresponding *R*-space plots during *p*-NP reduction. (C) Ni K-edge XANES and (D) corresponding *R*-space plots during *p*-NP reduction.

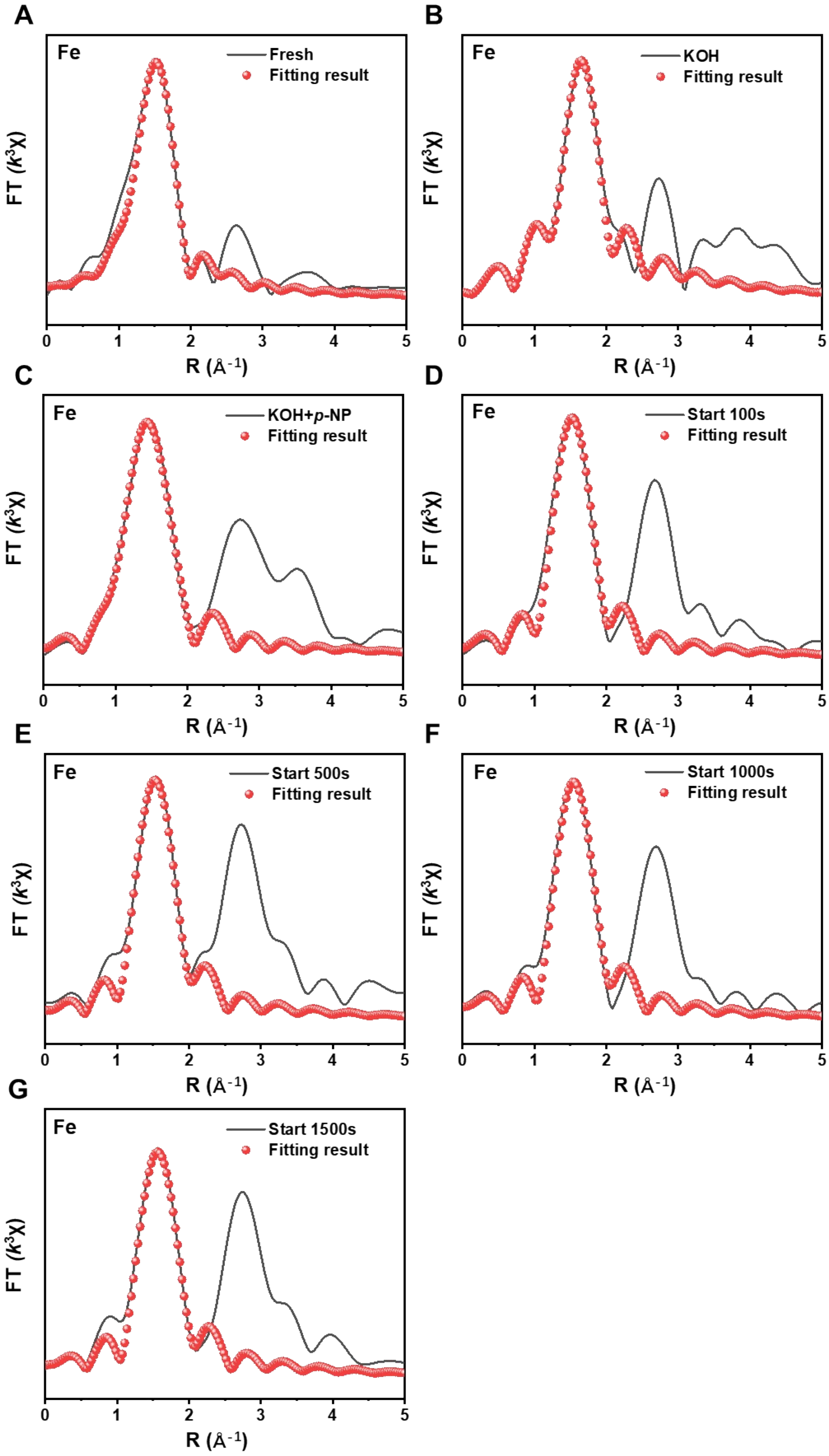

Figure S14. *In-situ* Fe K-edge *R*-space plots with corresponding fitting results for NiFe-400 at different stages of the *p*-NP reduction reaction.

Table S4. Local structure parameters around Fe estimated by *in-situ* EXAFS analysis for NiFe-400 at stages of the *p*-NP reduction reaction.

sample	**shell**	***N***	***R*(Å)**	**σ^2(10^{-3} Å^2)**	***R*-factor(10^{-3})**
Fresh	Fe-O	3.96	1.97	9.00	12.3
KOH	Fe-O	4.42	2.04	1.75	10.4
KOH+ *p*-NP	Fe-O	4.67	2.01	1.00	13.6
Start 100s	Fe-O	4.71	2.00	1.05	11.8
Start 500s	Fe-O	4.74	2.00	0.10	9.42
Start 1000s	Fe-O	4.74	2.01	0.15	11.63
Start 1500s	Fe-O	4.75	2.02	0.15	4.44

N = coordination number; *R* = average distance between absorber and backscatter atoms; σ^2 = Debye-Waller factor.

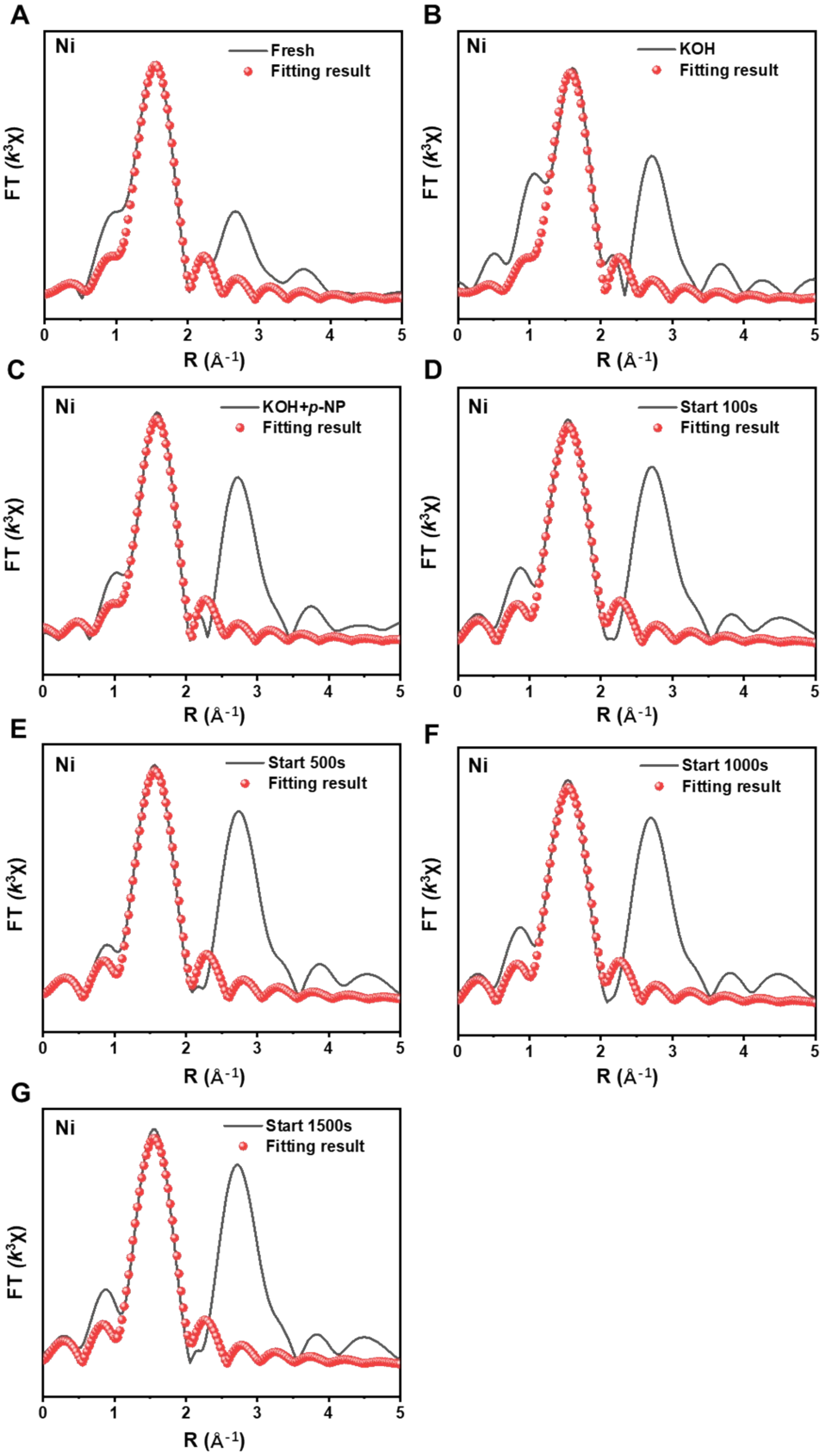

Figure S15. *In-situ* Ni K-edge *R*-space plots with corresponding fitting results for NiFe-400 at different stages of the p-NP reduction reaction.

Table S5. Local structure parameters around Ni estimated by *in-situ* EXAFS analysis for NiFe-400 at different stages of the p-NP reduction reaction.

Sample	**Shell**	***N***	***R*(Å)**	**σ^2(10^{-3} Å^2)**	***R*-factor(10^{-3})**
Fresh	Ni-O	4.64	2.02	5.00	10.0
KOH	Ni-O	4.63	2.05	5.20	16.0
KOH+ *p*-NP	Ni-O	4.67	2.05	5.30	5.67
Start 100s	Ni-O	4.69	2.04	3.15	7.21
Start 500s	Ni-O	4.69	2.04	3.08	9.58
Start 1000s	Ni-O	4.70	2.04	3.18	10.6
Start 1500s	Ni-O	4.70	2.04	2.85	9.10

N= coordination number; *R*= average distance between absorber and backscatter atoms; σ^2 = Debye-Waller factor.

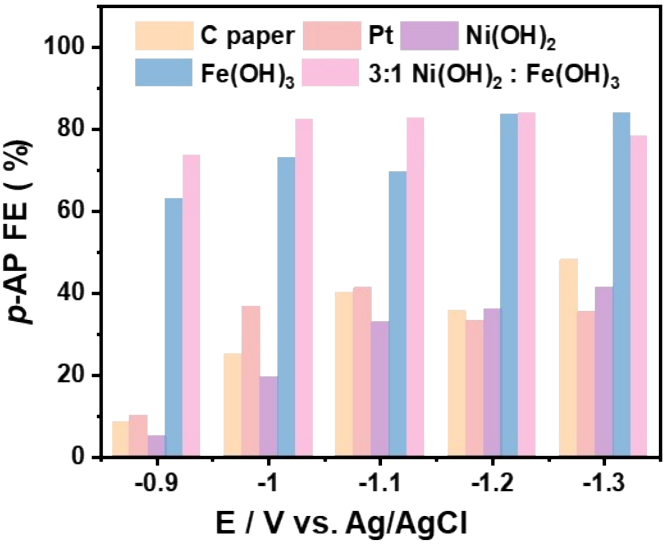

Figure S16. FE of *p*-AP over C paper, Pt, Ni(OH)$_2$, Fe(OH)$_3$ and a mixed catalyst (3:1 Ni(OH)$_2$: Fe(OH)$_3$) at various potentials from -0.9 to -1.3 V *vs*. Ag/AgCl, respectively.

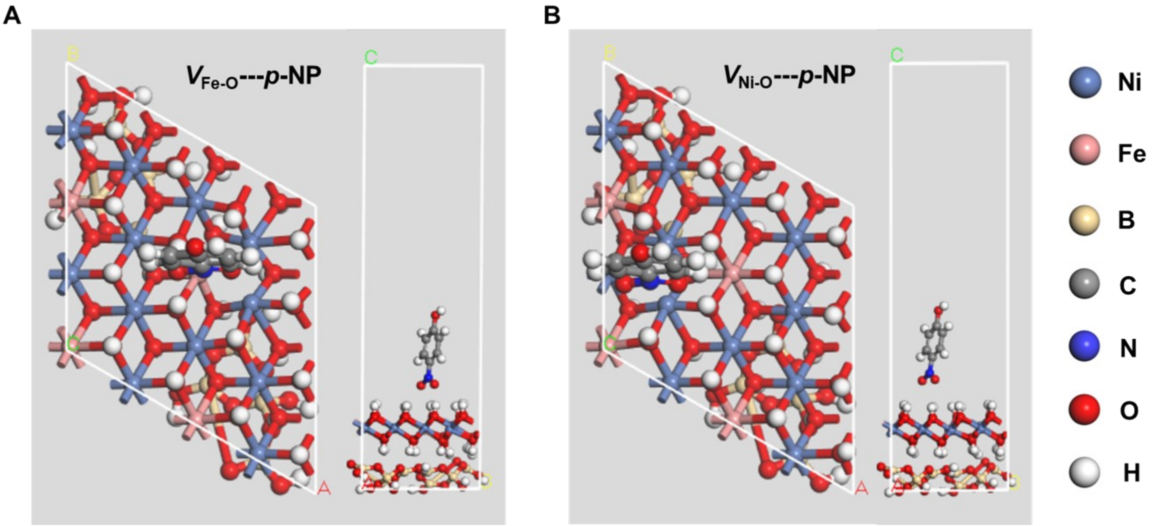

Figure S17. Illustration of the optimized geometry of *p*-NP on Fe site and Ni site of NiFe-LDH.

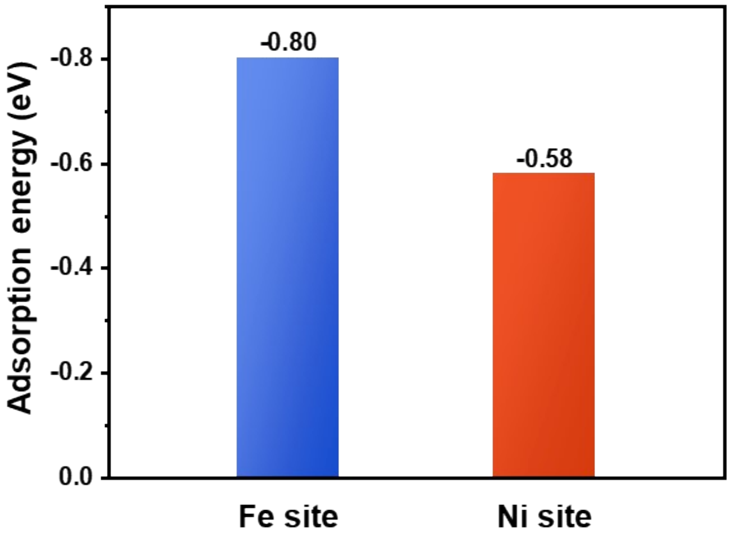

Figure S18. Adsorption energies of *p*-NP on Fe site and Ni site of NiFe-LDH.

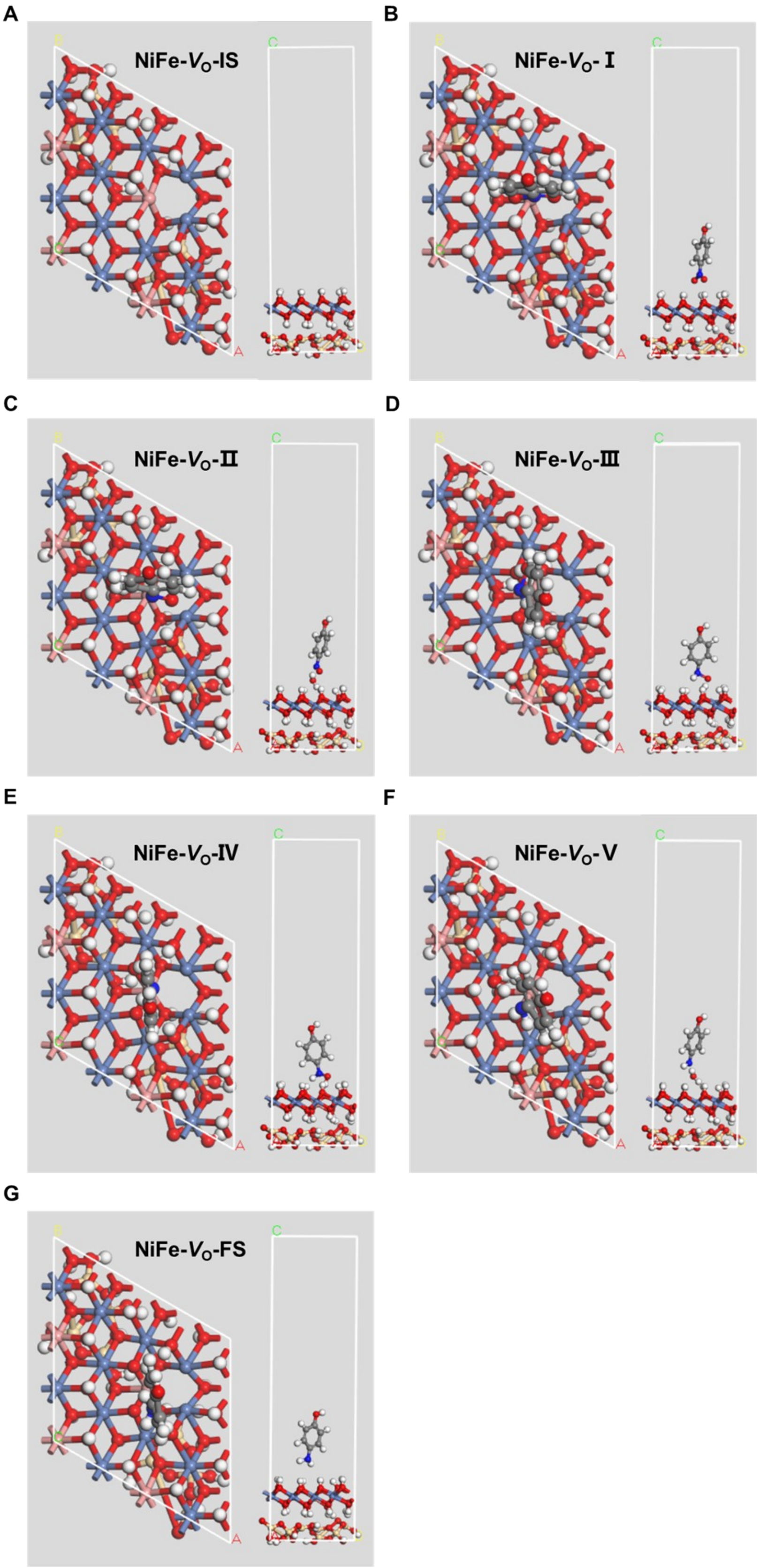

Figure S19. Optimization of the reaction path for *p*-NP hydrogenation over NiFe-LDH-V_O.

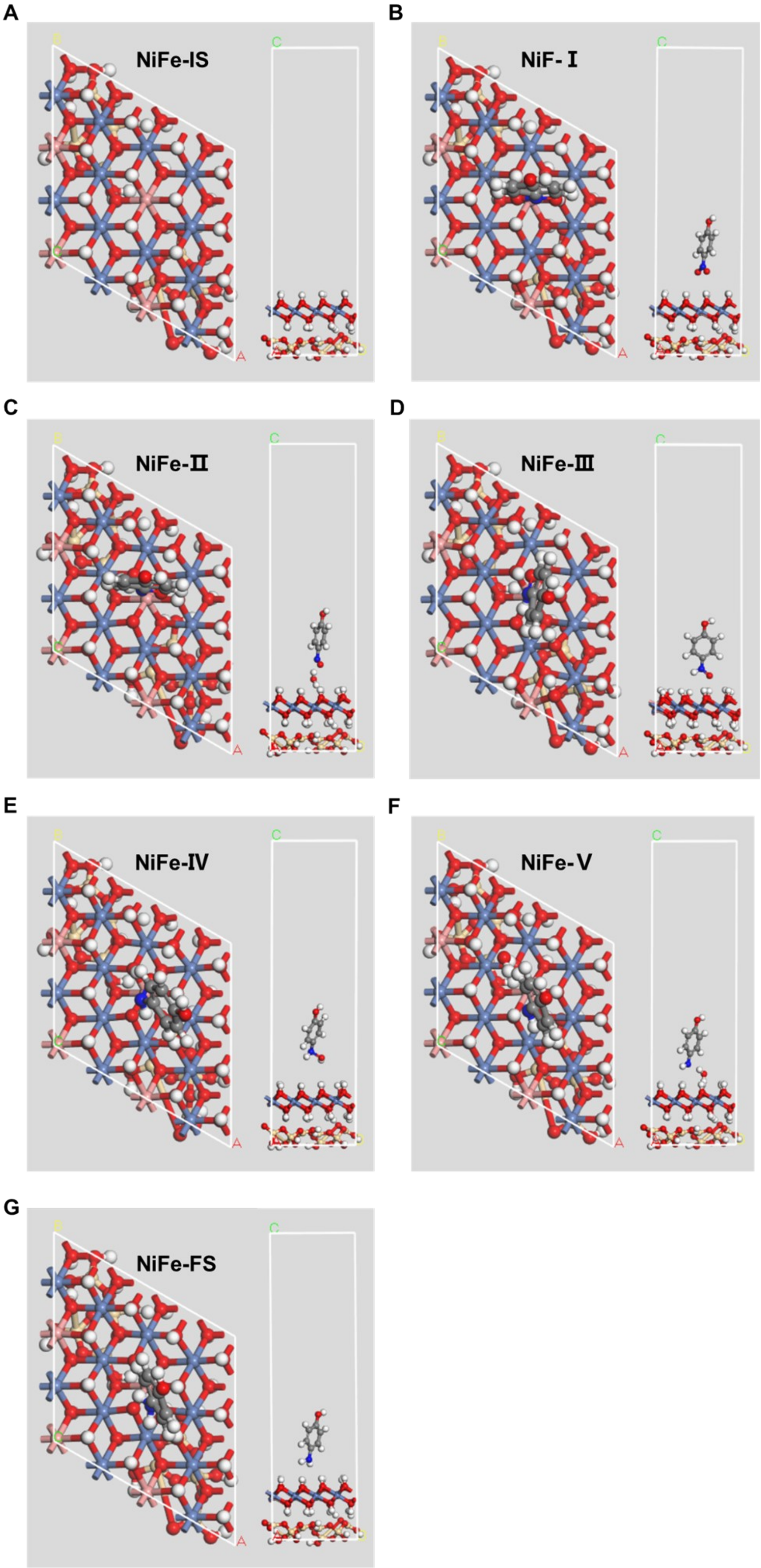

Figure S20. Optimization of the reaction path for *p*-NP hydrogenation over NiFe-LDH.

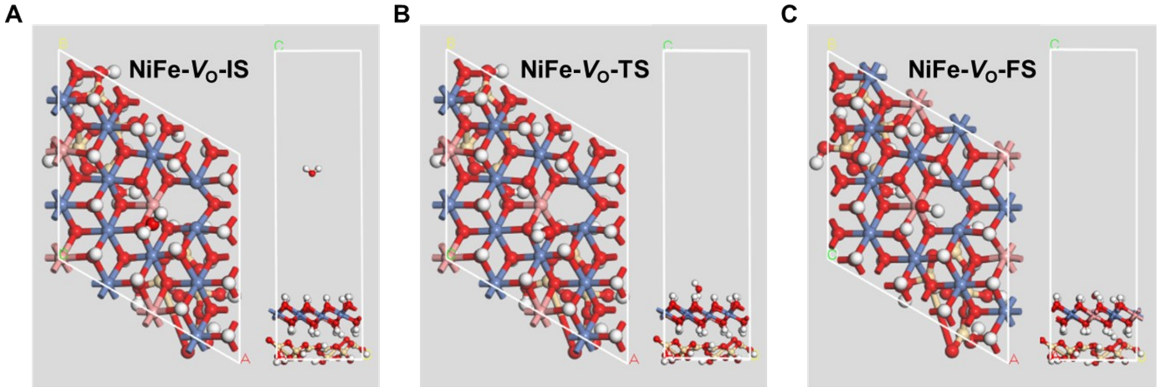

Figure S21. Optimized pathways for H* formation from H_2O dissociation on NiFe-LDH-V_O. IS initial state, TS transition state, FS final state.

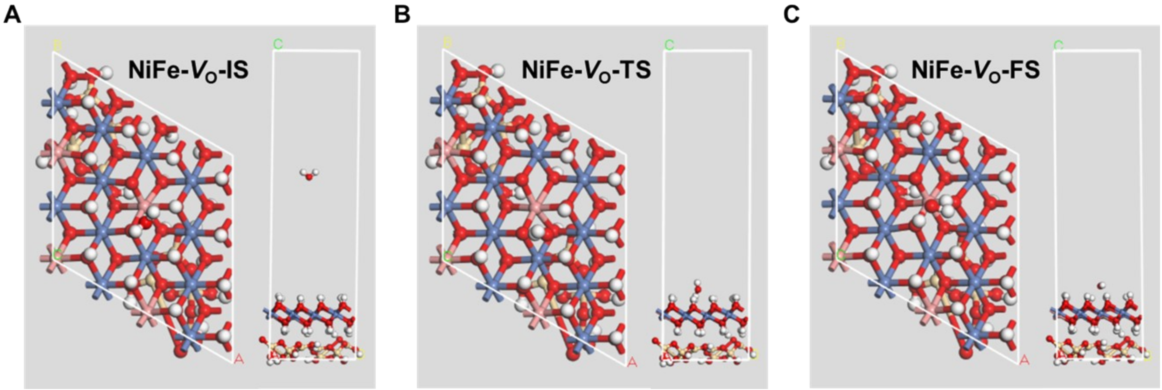

Figure S22. Optimized pathways for H* formation from H_2O dissociation on NiFe-LDH. IS initial state, TS transition state, FS final state.

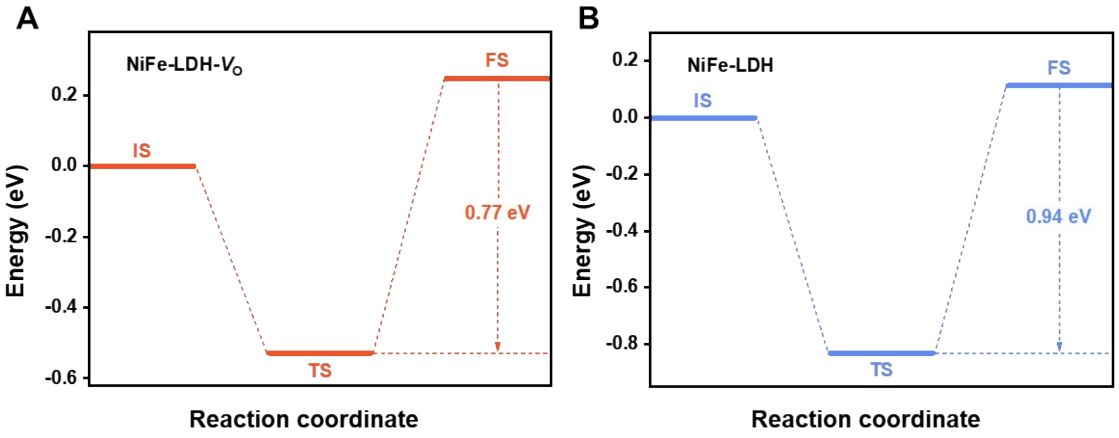

Figure S23. Energies profiles for H_2O dissociation on (A) NiFe-LDH-V_O and (B) NiFe-LDH.

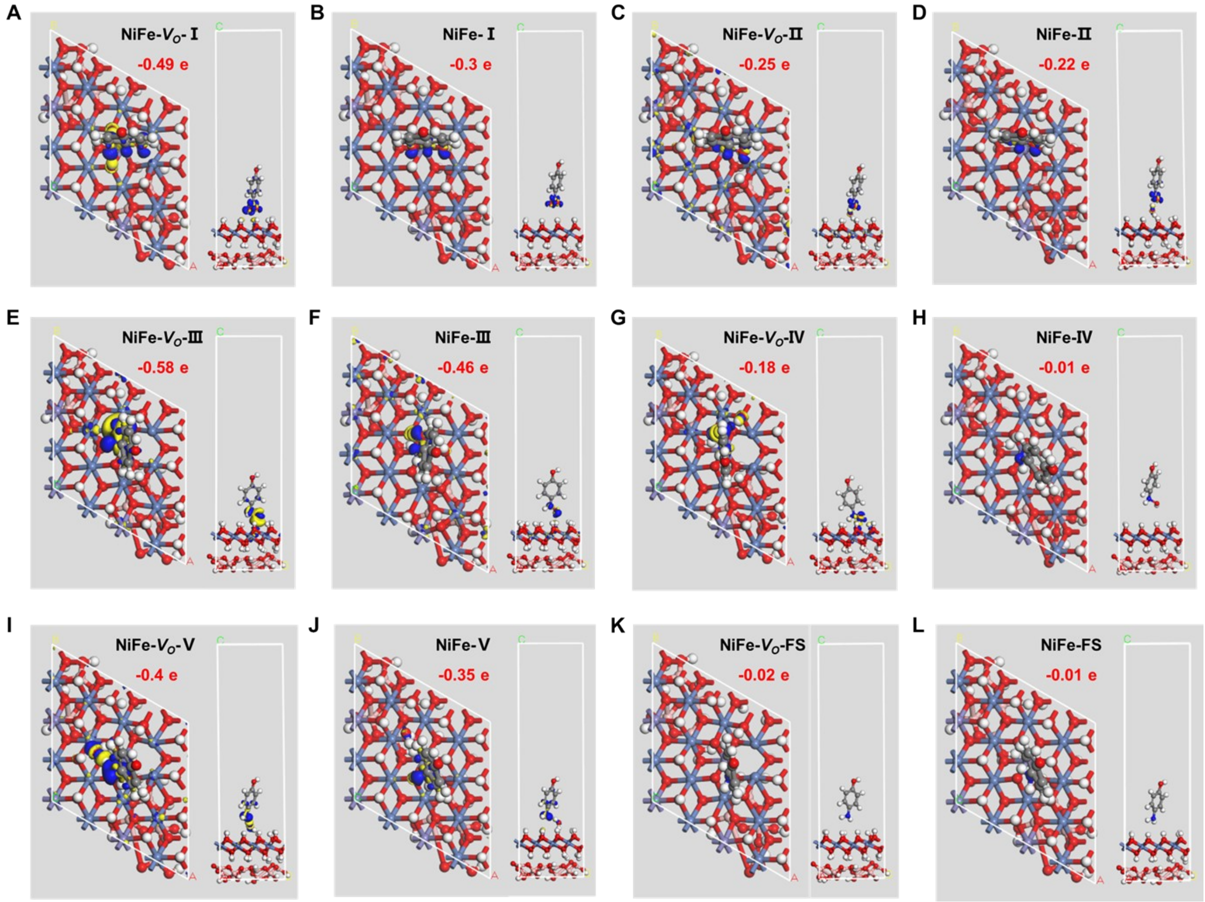

Figure S24. Differential charge density analysis for *p*-NP hydrogenation over NiFe-LDH-V_O and NiFe-LDH.

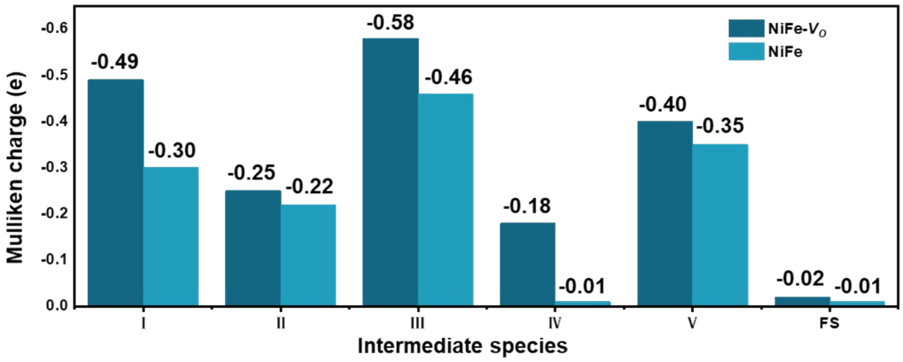

Figure S25. Mulliken charge for *p*-NP hydrogenation over NiFe-LDH-V_O and NiFe-LDH.

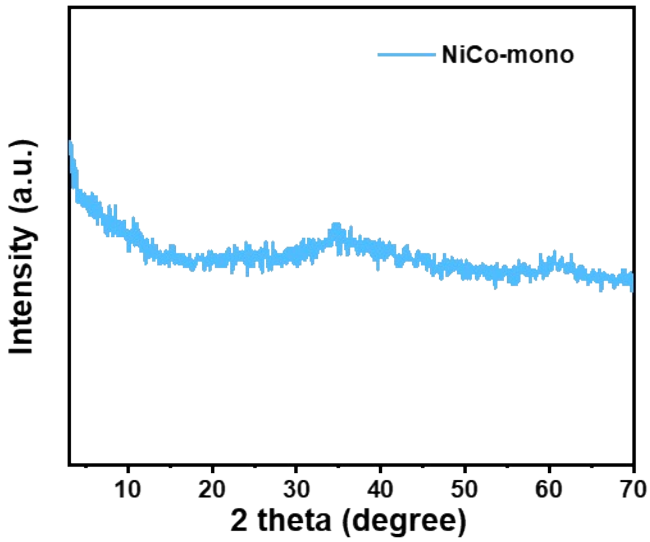

Figure S26. XRD pattern for NiCo-mono.

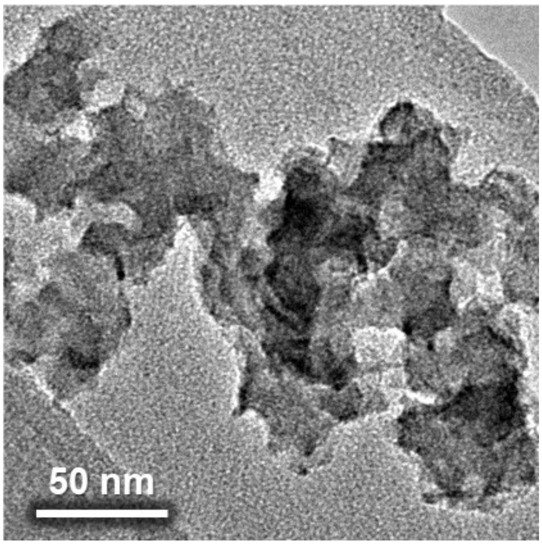

Figure S27. HRTEM image of NiCo-mono.

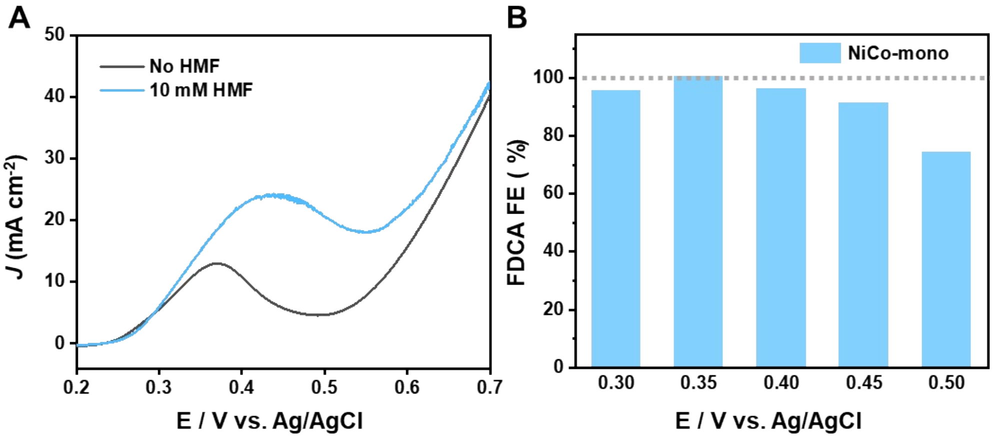

Figure S28. (A) LSV curves for NiCo-mono collected at a scan rate of 5 mV s^{-1} in 1.0 M KOH with and without 10 mM HMF. (B) FE of FDCA over NiCo-mono at various potentials from 0.30 to 0.50 V *vs*. Ag/AgCl.

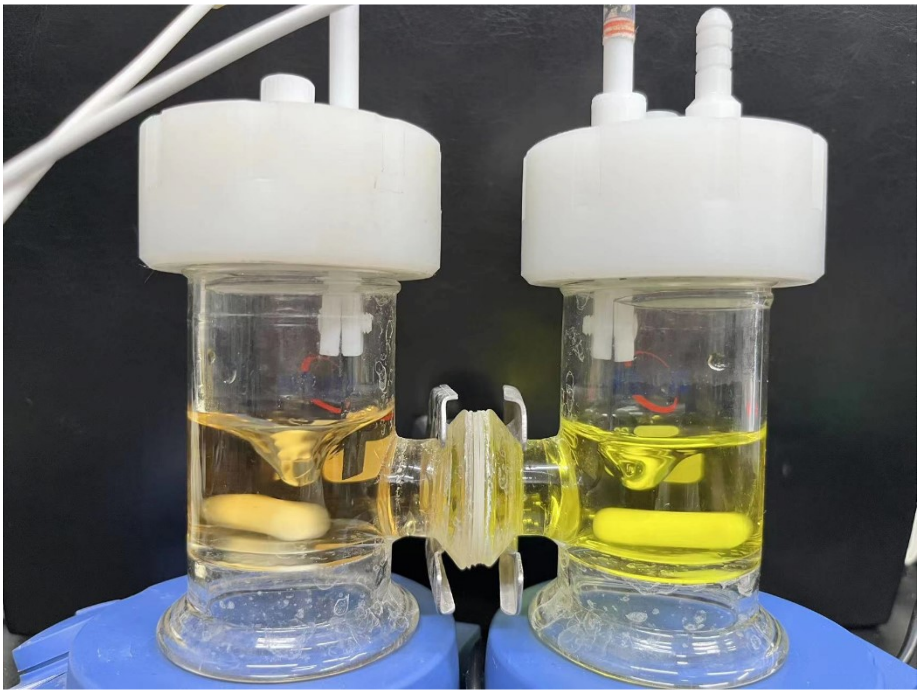

Figure S29. Photograph of the electrochemical H-cell, with (left) HMF oxidation at the NiCo-mono anode, and (right) *p*-NP reduction at the NiFe-400 cathode. The catholyte was 1.0 M KOH containing 10 mM HMF, and the anolyte 1.0 M KOH containing 10 mM *p*-NP.

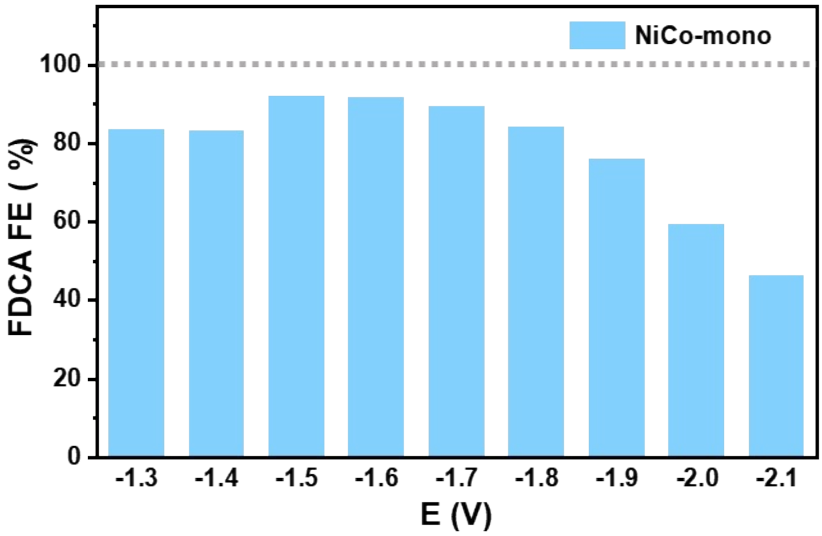

Figure S30. FE of FDCA using the paired electrolyzer at various potentials from -1.3 to -2.1 V of full voltage, respectively.

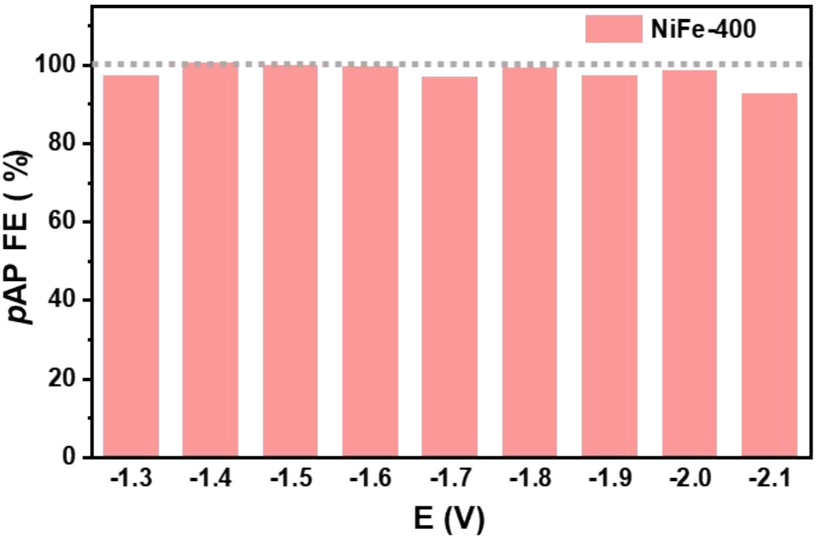

Figure S31. FE of *p*-AP using the paired electrolyzer at various potentials from -1.3 to -2.1 V of full voltage, respectively.

References

1. P. Li, X. Duan, Y. Kuang, Y. Li, G. Zhang, W. Liu and X. Sun, *Adv. Energy Mater.*, 2018, **8**, 1703341.
2. N. Wang, Z. Cao, X. Kong, J. Liang, Q. Zhang, L. Zheng, C. Wei, X. Chen, Y. Zhao, L. Cavallo, B. Zhang and X. Zhang, *J. Mater. Chem. A*, 2018, **6**, 16959-16964.
3. J. Lv, L. Wang, R. Li, K. Zhang, D. Zhao, Y. Li, X. Li, X. Huang and G. Wang, *ACS Catal.*, 2021, **11**, 14338-14351.
4. Y. Wang, C. Jiang, Y. Le, B. Cheng and J. Yu, *Chem. Eng. J.*, 2019, **365**, 378-388.
5. S. Guo, Y. Wu, C. Wang, Y. Gao, M. Li, B. Zhang and C. Liu, *Nat. Commun.*, 2022, **13**, 5297.
6. M. Li, C. Liu, Y. Huang, S. Han and B. Zhang, *Chin. J. Catal.*, 2021, **42**, 1983-1991.
7. S. Huang, Y. Jin, M. Zhang, K. Yan, S.-P. Feng and J. C.-H. Lam, *Green Chem.*, 2022, **24**, 7974-7987.
8. X. H. Chadderdon, D. J. Chadderdon, T. Pfennig, B. H. Shanks and W. Li, *Green Chem.*, 2019, **21**, 6210-6219.
9. K. Ji, M. Xu, S.-M. Xu, Y. Wang, R. Ge, X. Hu, X. Sun and H. Duan, *Angew. Chem. Int. Ed.*, 2022, **61**, e202209849.
10. T. Peng, T. Zhuang, Y. Yan, J. Qian, G. R. Dick, J. Behaghel de Bueren, S.-F. Hung, Y. Zhang, Z. Wang, J. Wicks, F. P. Garcia de Arquer, J. Abed, N. Wang, A. Sedighian Rasouli, G. Lee, M. Wang, D. He, Z. Wang, Z. Liang, L. Song, X. Wang, B. Chen, A. Ozden, Y. Lum, W. R. Leow, M. Luo, D. M. Meira, A. H. Ip, J. S. Luterbacher, W. Zhao and E. H. Sargent, *J. Am. Chem. Soc.*, 2021, **143**, 17226-17235.
11. M. Wang, T. Peng, C. Yang, B. Liang, H. Chen, M. Kumar, Y. Zhang and W. Zhao, *Green Chem.*, 2022, **24**, 142-146.
12. Q. Yang, B. Ge, P. Yuan, S. Luo, H. Zhang, Z. Zhao, J. Zhang, S. Wang, X. Bao and X. Yao, *Adv. Funct. Mater.*, 2023, DOI: 10.1002/adfm.202214588, 2214588.
13. W. Zhang, W. Zhang, J. Tan, D. Pan, Y. Tang and Q. Gao, *J. Mater. Chem. A*, 2023, **11**, 7505-7512.
14. X. Chong, C. Liu, Y. Huang, C. Huang and B. Zhang, *Natl. Sci. Rev.*, 2019, **7**, 285-295.
15. Y. Zhao, C. Liu, C. Wang, X. Chong and B. Zhang, *CCS Chem.*, 2021, **3**, 507-515.
16. M. Liu, A. Kong, J. Zhang, Y. Fu and W. Li, *Int. J. Hydrogen Energy*, 2022, **47**, 2187-2199.
17. P. Zhang, X. Sheng, X. Chen, Z. Fang, J. Jiang, M. Wang, F. Li, L. Fan, Y. Ren, B. Zhang, B. J. J. Timmer, M. S. G. Ahlquist and L. Sun, *Angew. Chem. Int. Ed.*, 2019, **58**, 9155-9159.
18. X. Pang, H. Bai, H. Zhao, W. Fan and W. Shi, *ACS Catal.*, 2022, **12**, 1545-1557.
19. S. Wu, X. Huang, H. Zhang, Z. Wei and M. Wang, *ACS Catal.*, 2021, **12**, 58-65.